CrossMark

CAMBRIDGE
UNIVERSITY PRESS

Research Article

Dashing through the cluster: An X-ray to radio view of UGC 10420 undergoing ram-pressure stripping

Smriti Mahajan[1] , Kulinder Pal Singh[1], Juhi Tiwari[1] and Somak Raychaudhury[2,3]

[1]Department of Physical Sciences, Indian Institute for Science Education and Research Mohali- IISERM, Knowledge City, Manauli, 140306, Punjab, India, [2]Ashoka University, Rajiv Gandhi Education City, Sonepat, Haryana 131029, India and [3]Inter-University Centre for Astronomy and Astrophysics, Ganeshkhind, Pune, Maharashtra 411007, India

Abstract

We present multi-wavelength data and analysis, including new *FUV* AstroSat/UVIT observations of the spiral galaxy UGC 10420 ($z =$ 0.032), a member of the cluster Abell 2199. UGC 10420 is present on the edge of the X-ray emitting region of the cluster at a distance of $\sim$680 kpc from the centre. The far-ultraviolet (*FUV*) data obtained by the *AstroSat* mission show intense knots of star formation on the leading edge of the galaxy, accompanied by a tail of the same on the diametrically opposite side. Our analysis shows that the images of the galaxy disc in the optical and mid-infrared are much smaller in size than that in the *FUV*. While the broadband optical colours of UGC 10420 are typical of a post-starburst galaxy, the star formation rate (SFR) derived from a UV-to-IR spectral energy distribution is at least a factor of nine higher than that expected for a star-forming field galaxy of similar mass at its redshift. A careful removal of the contribution of the diffuse intracluster gas shows that the significant diffuse X-ray emission associated with the interstellar medium of UGC 10420 has a temperature, $T_X = 0.24^{+0.09}_{-0.06}$ keV (0.4–2.0 keV) and luminosity, $L_X = 1.8 \pm 0.9 \times 10^{40}$ erg s^{-1}, which are typical of the X-ray emission from late-type spiral galaxies. Two symmetrically placed X-ray hot spots are observed on either sides of an X-ray weak nucleus.

Our analysis favours a scenario where the interaction of a galaxy with the hot intracluster medium of the cluster, perturbs the gas in the galaxy causing starburst in the leading edge of the disc. On the other hand, the turbulence thus developed may also push some of the gas out of the disc. Interactions between the gas ejected from the galaxy and the intracluster medium can then locally trigger star formation in the wake of the galaxy experiencing ram-pressure stripping. Our data however does not rule out the possibility of a flyby encounter with a neighbouring galaxy, although no relevant candidates are observed in the vicinity of UGC 10420.

Keyword: galaxies: evolution – galaxies: fundamental parameters – galaxies: star formation – galaxies: individual: UGC 10420

1. Introduction

The evolution of galaxies is often accelerated in the vicinity of galaxy clusters due to the presence of hot intra-cluster medium (ICM), and close proximity to large neighbouring galaxies. For several decades astronomers have focused on understanding the various mechanisms responsible for the morphology–density relation (Dressler, 1980) and star formation–density relation (e.g. Balogh et al., 2004) of galaxies. These mechanisms are believed to be the reason for the presence of more red, elliptical and passively evolving galaxies in and near clusters, relative to their counterparts farther away from the cluster centres.

Gravitational and tidal interactions with comparable-sized neighbours (Toomre & Toomre, 1972; Moore et al., 1996), emerge as the most important processes leading to the depletion of gas in galaxies residing in intermediate density environments such as the cluster outskirts and large-scale filaments (e.g. Porter & Raychaudhury, 2005; Mahajan et al., 2010, 2012). On the other hand, ram-pressure stripping (RPS; Gunn & Gott, 1972) plays a

significant role in the evolution of galaxies in the dense interiors of clusters and groups. The hydrodynamical interaction of the cold gas in a galaxy with the hot ICM can lead to the evaporation of the interstellar medium (ISM; Cowie & Songaila, 1977), or complete removal of it from the galaxy via RPS. As a consequence, such a galaxy will eventually cease to form new stars, turn optically red and become elliptical on timescales of $\sim$1 Gyr. This idea is in agreement with the presence of a large number of HI-deficient galaxies in nearby clusters (e.g. Gavazzi et al., 2006; Haines et al., 2009; Vulcani et al., 2010; Boselli et al., 2014; Cybulski et al., 2014).

Hydrodynamical simulations, however suggest that in the initial phase, for a short but significant duration of time RPS can lead to enhancement in the star formation rate (SFR) of galaxies (Bekki & Couch, 2003; Bekki, 2014; Steinhauser et al., 2016; Lee et al., 2020; Troncoso-Iribarren et al., 2020). Using multi-wavelength datasets, several incidences of starbursts occurring in RPS galaxies have now been confirmed in nearby clusters (e.g. Crowl et al., 2006; Yagi et al., 2010; Gavazzi et al., 2015; Vulcani et al., 2018; Boselli et al., 2022; Lee et al., 2022). In a systematic study of RPS candidates at low-redshift, Poggianti et al. (2016) found that at fixed mass, these galaxies have at least twice the rate of star formation relative to unstripped galaxies.

The environmental processes such as RPS, which influence the gas content of a galaxy can also impact its nuclear activity. The idea

is based on the observations of enhanced star formation among galaxies experiencing RPS. Due to the turbulence and instabilities in the disc, resulting from the interaction of the galaxy with the intracluster medium, gas can be funnelled in towards the galaxy's centre. This gas can thereby ignite the central supermassive black hole (Tonnesen & Bryan, 2009), although observational evidence in favour of these ideas appear debatable at present. In a recent study of nearby galaxies, a high incidence of optical AGN was found to be present among RPS galaxies relative to a mass-matched control sample (Peluso et al., 2022). However, Cattorini et al. (2022) suggest that the results of Peluso et al. (2022) may be biased by the fact that they are considering both Seyfert and low-ionisation narrow-emission-line region (LINERs) as AGN, and they are evaluating the AGN fraction with respect to the emission-line galaxies only. RPS can also have a significant effect on the surface brightness, temperature and metallicity of the hot ISM of a galaxy (Kapferer et al., 2009).

In this paper, we present multi-wavelength data and analysis, including new far-ultraviolet (*FUV*) observations from AstroSat/UVIT for the RPS galaxy UGC 10420 which is a member of the cluster Abell 2199 ($z = 0.031$) and has been observed in many wavebands from X-ray to radio. Some empirical facts about the X-ray cluster Abell 2199, sourced from Rines et al. (2016) are provided in Table 2, while physical properties of UGC 10420 compiled from the literature, or derived for this analysis, are listed in Table 3. It is noteworthy that UGC 10420 has a very small radial offset with the cluster's mean line-of-sight (l.o.s.) velocity, such that $\Delta v \sim 372$ km s^{-1}. The structure of the paper is as follows: in the following section we describe various observations and data used in this paper, followed by our analysis in § 3. In § 4, we discuss the results in the context of the existing literature and finally conclude the paper with an epilogue in § 5. Throughout this work we use concordance Λ cold dark matter cosmological model with $H_0 = 70$ km s^{-1} Mpc^{-1}, $\Omega_\Lambda = 0.7$, and $\Omega_m = 0.3$ to calculate distances and magnitudes.

2. Observations and data reduction

In this section we describe the source and properties of data compiled for UGC 10420.

2.1. Ultraviolet data

UGC 10420 was observed with the ultraviolet imaging telescope (UVIT) aboard the *AstroSat* mission (Kumar et al., 2012; Singh et al., 2014; Tandon et al., 2017). This field (observation ID: A05_063T03_9000003066; PI: Smriti Mahajan; observation date: 30-July-2019) was observed by the UVIT simultaneously in the broadband BaF2 *FUV* filter (mean $\lambda = 1541$ Å; $\Delta\lambda = 380$ Å; Tandon et al., 2017, 2020), and visible wavebands (3040 − 5500 Å), although the latter data have not been used for scientific analysis here. The raw data from the mission are processed by the Indian Space Science Data Centre (ISSDC), and the Level 1 data from all instruments are provided to the users. A more comprehensive account of processing of data and analysis of this field will be presented in an accompanying paper (Mahajan et al., in preparation), but is briefly mentioned below for completion.

The UVIT data used in this paper have a total exposure time of 9600.3 seconds and resolution of <1.2″. The L1 data were processed using the CCDLAB software (Postma & Leahy, 2017),
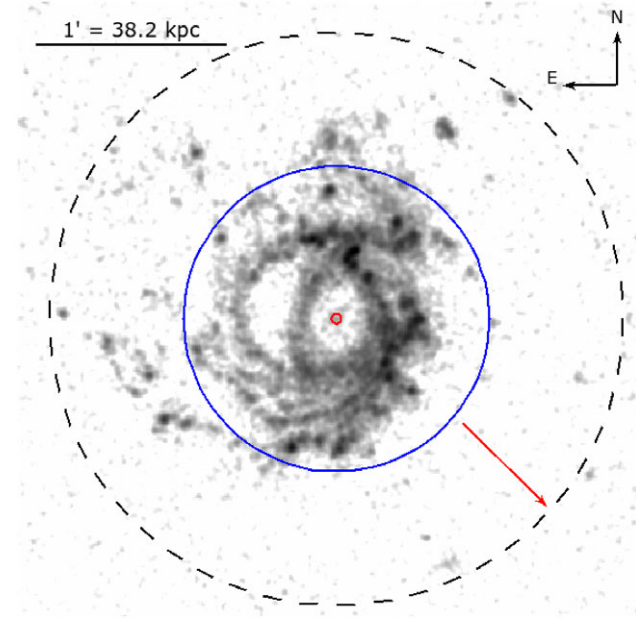

Figure 1. This is the AstroSat/UVIT image of UGC 10420. The small *red circle* represents the 3″ diameter SDSS fibre drawn on the optical centre of the galaxy. The spectrum obtained from this region is shown in Fig. 5, and represents a broadline emission region. The *solid blue* and *dashed black* circles having radius of 0.8′ and 1.5′, respectively, are shown for reference to represent the region used for photometric measurements in various filters. The arrow points in the direction of the cluster centre.

following the procedure described in Postma & Leahy (2021, also see Mahajan et al. (2022) for a step-wise account of creating science images of similar data). The final UVIT *FUV* image of UGC 10420 is shown in Fig. 1. For comparison, we show two circles of radii 0.8′ and 1.5′, respectively. While the 1.5′ region better captures the UV emission of UGC 10420, the smaller circle is a better representation of the size of the galaxy at longer wavebands, as shown below.

UGC 10420 was also observed by the Galaxy and Mass Evolution Explorer (*GALEX*) in the near and far ultraviolet broadbands as shown in Fig. 2 (left). It is noteworthy that the shallow exposure time and poor resolution renders this image unimpressive relative to the UVIT counterpart shown in Fig. 1. These data were taken as part of *GALEX*'s medium imaging survey (MIS) and have a total exposure time of 1649.1 seconds in both the bands.

In order to measure the flux from UGC 10420, an aperture had to be chosen manually because the commonly used software split the galaxy into multiple components due to its large size and discontinuous emission in almost all filters. The aperture photometry was performed using the SAOImageDS9 software package (Joye & Mandel, 2003), by choosing an aperture size of 1.5′ centred at the optical nucleus (α: 16h29m51.04s; δ: +39d45m59.42s) for all three UV images. First, we estimated the background counts by averaging over multiple source-free circular regions of radius ≥ 1.5′ and subtracted them from the counts obtained for the region centred on UGC 10420. The counts were then converted to fluxes using the standard conversion factors given in Tandon et al. (2020) for the UVIT image, and https://asd.gsfc.nasa.gov/archive/galex/FAQ/counts_background.html for the *GALEX* images, respectively. The final flux values, measurement uncertainty in flux, and the effective wavelength for all wavebands are listed in Table 1.
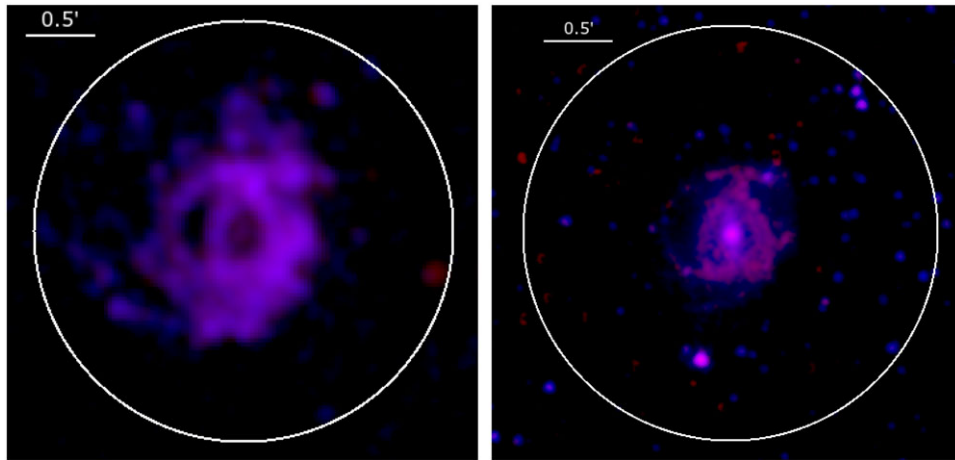
Figure 2. *(left:)* The *GALEX* image of UGC 10420 where *blue* and *red* represent the *FUV* and *NUV* broadband images, respectively. *(right:)* This composite image of UGC 10420 shows the NIR emission in the IRAC 3.6 μm *(blue)* and 5.8 μm *(red)* bands. A circle of 1.5′ radius is shown in both the images for comparison. It is evident that the image of the galaxy is much smaller in the infrared bands.

2.2. X-ray Data

UGC 10420 was in the field of view of an observation with the *XMM-Newton* EPIC[a]. This observation (Obs. ID: 0784521201, PI: Takayuki Tamura, Obs. time: 40 ks) carried out on 2017 March 17 was centred at α: 16h30m32s and δ: +39d44m52s and focused on the intermediate regions ($<3/4$ virial radius) of Abell 2199. All the three detectors aboard *XMM-Newton*, viz., EPIC PN, MOS1 amd MOS2 detectors were operated in the Full Frame mode and medium optical blocking filter was used. The dataset for this observation was retrieved from the HEASARC[b] archive, then processed and analysed using the *XMM-Newton* Science Analysis System (SAS) version 20.0.0 and the Extended Source Analysis Software (XMM-ESAS) package integrated into SAS. The latest calibration files were employed to produce the PN (MOS) event files using the SAS tasks *epchain* (*emchain*).

The X-ray data were first screened to remove the particle backgrounds as described below:

a) The event files were filtered for soft proton (SP) background flares using the tasks *pn-filter* and *mos-filter*. The SP flare filtering resulted in useful exposure times of 28.92, 35.46, and 38.20 ks for the PN, MOS1, and MOS2 detectors, respectively. We examined the output of the task *mos-filter* and verified that none of the MOS detectors operated in an anomalous state during the observation.

b) The events arising due to quiescent particle background (QPB) produced by the interaction of high energy particles (>100 MeV) with the X-ray detectors and the surrounding structure was then removed. QPB shows only small intensity variations over the time scale of a typical X-ray observation and therefore not detected as flares. The standard norm to subtract out the QPB contribution from the data is to either use blanksky observations or model the QPB. The XMM-ESAS package models the QPB using a combination of a database of unexposed-region data and filter-wheel-closed data based on

the methods of Kuntz & Snowden ([2008](#)), and we have used this method to model and subtract the QPB instead of using blanksky files.

The filtered event files thus produced were used for making the images and spectra and analysed as described below.

The XMM-ESAS tasks *pn-spectra* (*mos-spectra*) followed by *pn_back* (*mos_back*) were used to generate the PN (MOS1/MOS2) images of UGC 10420 in three different energy bands (one at a time), viz. soft: $400 - 2000$ eV, hard: $2000 - 7000$ eV, and total: $400 - 7000$ eV, by setting the *elow* and *ehigh* energy parameters to the requisite values (unit: eV). These tasks also generated the QPB images and exposure maps for each EPIC detector. The individual PN, MOS1, and MOS2 counts images, exposure maps, and model QPB images were then combined into a single counts, exposure, and QPB image using the task *comb*. Finally, a combined PN, MOS1, and MOS2 particle-background-subtracted, exposure-corrected, and adaptively smoothed surface brightness image of UGC 10420 was generated using the task *adapt*. A smoothing scale of 10 counts and a pixel size of 2.5″ were used. X-ray images of UGC 10420 in the three energy bands are shown in [Figure 4](#). The nuclear region around the optical centre appears to be very faint and soft in X-rays, with two bright spots, neither of which is coincident with the optical centre, and surrounded by some diffuse emission. Emission from the central region cannot be seen in the hard X-ray band, however. The two bright sources far away from the nuclear region on the east and west are confirmed as point sources using the ESAS task *cheese*, which runs point source detection by calling the SAS task *edetect_chain*. We used a detection box of 5×5 pixels for this purpose. Further analysis of these X-ray sources is presented in [§ 3.3](#).

2.3. Optical data

The optical photometric and spectroscopic data used in this paper are sourced from the Sloan Digital Sky Survey (SDSS, data release 14; Abolfathi et al., [2018](#)), unless mentioned otherwise. The SDSS images have an exposure time of 53.9 seconds in each of the five filters u, g, r, i, z. Photometry was performed in all five wavebands using an aperture size of 0.8′, following the procedure described in

---

[a]The European Photon Imaging Camera onboard the XMM-Newton observatory.
[b]High Energy Astrophysics Science Archive Research Center; https://heasarc.gsfc.nasa.gov/

Table 1. Integrated flux measurements for UGC 10420 in different wavebands, in increasing order of wavelength from top to bottom.

Filter	Effective λ	Flux	Uncertainty in flux	Source
	(Å)	(mJy)	(mJy)	
GALEX FUV	0.152	1.486	4.00E−01	measured from image
UVIT BaF2	0.154	2.030	8.04E−03	measured from image
GALEX NUV	0.232	2.315	2.90E−01	measured from image
SDSS *u*	0.356	2.573	9.66E−02	measured from image
U	0.357	3.060	2.64E−00	from Gil de Paz et al. (2007)
B	0.446	6.877	5.99E−00	from Gil de Paz et al. (2007)
SDSS *g*	0.477	6.920	1.58E−01	measured from image
V	0.550	11.197	9.66E−00	from Gil de Paz et al. (2007)
SDSS *r*	0.623	11.410	2.03E−01	measured from image
SDSS *i*	0.763	15.438	2.37E−01	measured from image
SDSS *z*	0.913	18.375	2.58E−01	measured from image
J	1.200	18.370	17.87E−00	from Gil de Paz et al. (2007)
H	1.620	19.653	18.77E−00	from Gil de Paz et al. (2007)
K	2.200	12.767	11.86E−00	from Gil de Paz et al. (2007)
WISE *W1*	3.368	12.922	2.84E−02	measured from image
IRAC *I1*	3.560	14.254	3.76E−01	measured from image
WISE *W2*	4.618	7.653	2.14E−02	measured from image
IRAC *I3*	5.760	14.457	9.95E−01	measured from image
WISE *W3*	12.082	13.993	0.17E−00	measured from image
WISE *W4*	22.194	16.027	0.75E−00	measured from image
Radio 144 MHz	2.087E+10	74.670	0.17E−00	measured from image

Table 2. Empirical facts about Abell 2199 (Rines et al., 2016).

Parameter	Value
Right Ascension (J2000)	16 28 37.90
Declination (J2000)	+39 32 55.32
Redshift (z)	0.0309
Velocity dispersion (σ)	676^{+37}_{-32} km s^{-1}
M_{200}	$(2.39 \pm 0.77) \times 10^{14}$ M$_\odot$

Sec. 2.1. The measured counts were then converted to fluxes using the standard conversion factor from maggies to Jy and are listed in Table 1.

In Fig. 3 (left), we show the position of the galaxy relative to the centre of Abell 2199, on the digitised sky survey (DSS) image of the field. UGC 10420 is ∼680 kpc away from the cD galaxy NGC 6166 of the cluster. A composite *g*, *r*, *i* image of UGC 10420, shown in Fig. 3 (right), clearly shows the asymmetry in the spiral arms of UGC 10420, and the presence of a bar at the centre, in agreement with the morphological classification of type SB(c) (Buta, 2019). Even though the outer regions of UGC 10420 are optically blue, majority of the optical emission from the disc is dominated by red

Table 3. Observed properties of UGC 10420, a member galaxy of cluster Abell 2199.

Parameter	Value	Reference
Right Ascension (J2000)	16 29 51.04	SDSS database
Declination (J2000)	+39 45 59.42	SDSS database
Redshift (z)	0.03185	SDSS database
Luminosity distance (D_L)	139.7 h^{-1} Mpc	–
Scale (kpc/″)	0.636	–
Morphological type	SB(c)	Buta (2019)
Position angle (PA) of stellar bar	89.9°	Fraser-McKelvie et al. (2020)
Length of stellar bar	3.9 kpc	Fraser-McKelvie et al. (2020)
Petrosian 50% radius in *r*-band, $R_{50,r}$	18.2″	Fraser-McKelvie et al. (2020)
Milkyway extinction, $E(B-V)$	0.0085	Schlafly & Finkbeiner (2011)

stellar populations, as quantified by a colour value of $(g-r) \sim 0.8$ mag, which is typical for passively-evolving late-type galaxies (e.g. Mahajan & Raychaudhury, 2009; Song et al., 2017; Mahajan et al., 2020).

The optical spectrum of UGC 10420 obtained from the 3″ diameter SDSS fibre is shown in Fig. 5 (also see Fig. 1 for a comparison between the size of the fibre relative to the galaxy). On the basis of emission line fluxes obtained from this spectrum, UGC 10420 is classified as a LINER galaxy, using the BPT (Baldwin et al., 1981) emission-line diagnostic diagram (Toba et al., 2014).

2.4. Infrared data

The infrared (IR) observations for UGC 10420 were obtained from the Infrared Science Archive (IRSA) of the NASA Infrared Processing and Analysis Center (IPAC)[c]. For this work we used the images from the Wide-field Infrared Survey Explorer (WISE; Wright et al., 2010), as well as the Infrared Array Camera (IRAC) aboard the *Spitzer* mission.

WISE observed the sky in the near- and mid-infrared wavebands between 3.6 and 22 μm. We performed photometry on all the four band *ALLWISE* images, and channels 1 and 3 IRAC images (3.6 and 5.8 μm, respectively) in the same manner as described in sec. 2.1, but using an aperture of 0.8′. Our choice of aperture size is dictated by the fact that the UGC 10420's image is much smaller in these bands, and, the aperture of 1.5′ used for the UV data would include many galactic and extragalactic sources not visible in other bands, thereby contaminating the flux measurement. The estimated fluxes are listed in Table 1. A glimpse of the IR emission relative to the light in the optical and *FUV* filters can be seen in Fig. 2 (right) and Fig. 6. Figs. 1–3 and 5 show that the optical-IR emission is concentrated in the central region of the galaxy encompassing the nucleus and the stellar bar, where as the *FUV* emission dominates the outer regions of the galaxy.

2.5. Radio data

The radio image of UGC 10420 is obtained from the data release 2 of the ongoing LOw-Frequency ARray (LOFAR) Two-metre Sky

[c]https://irsa.ipac.caltech.edu/about.html
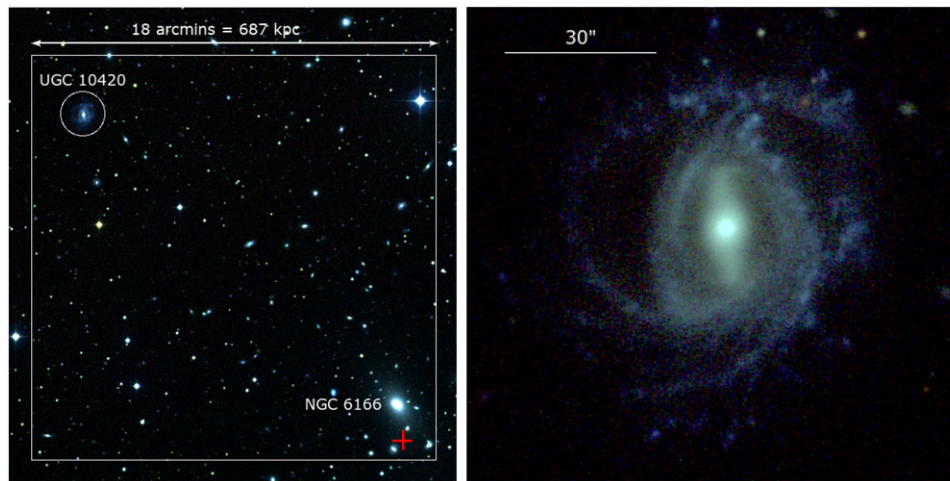
Figure 3. *(left:)* The combined *B*, *R*, and *I* band digitised sky survey (DSS) image of the sky around UGC 10420. The central elliptical galaxy of Abell 2199, NGC 6166 is marked along with the X-ray centre of the cluster (*red cross*; Mahdavi & Geller, 2001) at the bottom right to show the relative position of UGC 10420 in the cluster. *(right:)* This is an optical *g*, *r*, *i* image of UGC 10420 created using the SDSS photometric data. North is up and east is on the left for both images.
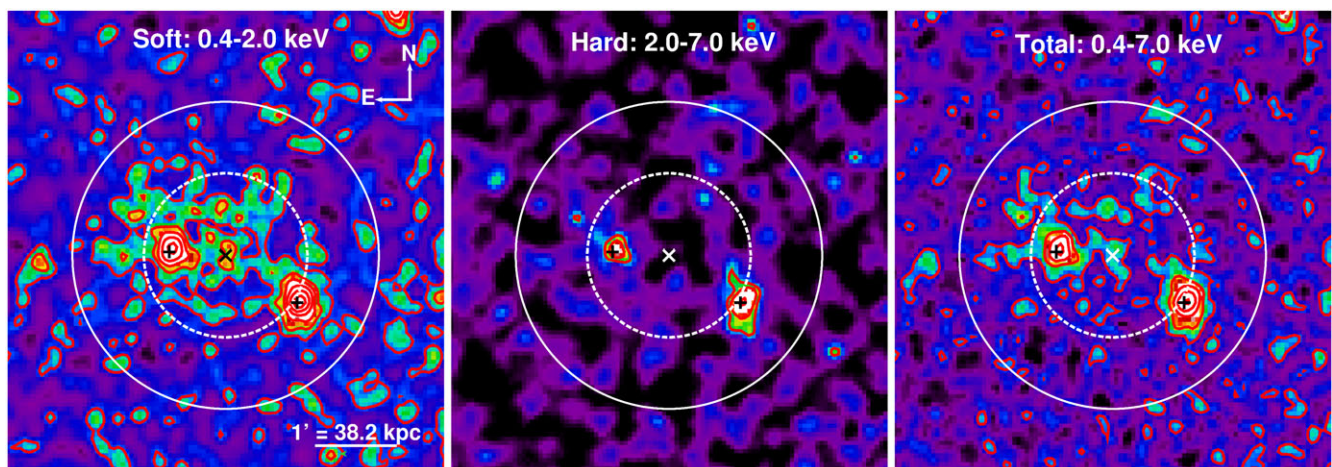
Figure 4. *left to right*: Particle-background-subtracted, exposure-corrected, combined PN, MOS1, and MOS2 *XMM-Newton* surface brightness image of UGC 10420 in the *soft* (0.4–2.0 keV), *hard* (2.0–7.0 keV), and *total* (0.4–7.0 keV) X-ray energy bands. The surface brightness contours are as follows – *soft band*: 6 levels (9.9, 20.9, 36.1, 61.1, 105.0, and 184.3 cts s^{-1} deg^{-2}) between 3σ and 88σ above a background level of 3.7 cts s^{-1} deg^{-2}; *hard band*: 3 levels (17.1, 30.8, and 81.3 cts s^{-1} deg^{-2}) between 3σ and 19σ above a background level of 5.1 cts s^{-1} deg^{-2}; *total band*: 5 levels (16.5, 43.9, 87.4, 172.8, and 350.2 cts s^{-1} deg^{-2}) between 3σ and 98σ above a background level of 6 cts s^{-1} deg^{-2}. In each panel, the $\times$ symbol marks the optical centre of UGC 10420, and the $+$ symbols mark the centres of the two X-ray point sources detected in the galaxy. The *solid white* and *dashed white* circles represent the 1.5′ and 0.8′ radius apertures, respectively, centred at the optical centre.

Survey (LoTSS; 120–168 MHz; Shimwell et al., 2022). The LoTSS images were derived from the LOFAR high band antenna data, which were corrected for the direction-independent instrumental properties as well as direction-dependent ionospheric distortions with fully automated, data processing. At $\sim$6″ resolution, the full bandwidth Stokes I continuum maps of these data at a central frequency of 144 MHz, have a median root mean square (rms) sensitivity of 83 μJy/beam, a flux density scale accuracy of approximately 10%, and astrometric accuracy of 0.2″.

The radio flux density mentioned in Table 1 was obtained using AIPS. In order to determine the flux density, the counts in a polygon region centred at UGC 10420 were determined and divided by the area covered by the beam. The uncertainty in the flux was calculated as the product of the square root of the number of beams within the polygon region, and the rms uncertainty

($=$ 0.017 mJy) in a similar sized source-free region. The flux density scale uncertainty for the LoTSS data is found to be $\sim$6% (Shimwell et al., 2022). The 144 MHz emission encompasses the optical disc of the galaxy as shown in an optical-UV-radio composite image of UGC 10420 in Fig. 7. The radio emission appears to be orientated along the direction of motion of the galaxy with a gap in the middle, in line with the *FUV* image of the galaxy (Fig. 1).

3. Analysis and results

3.1. Spectral energy distribution

The arsenal of data mentioned in Section 2 can be used to derive useful information about the stars, gas, and dust of UGC 10420 by means of its spectral energy distribution (SED). In this work
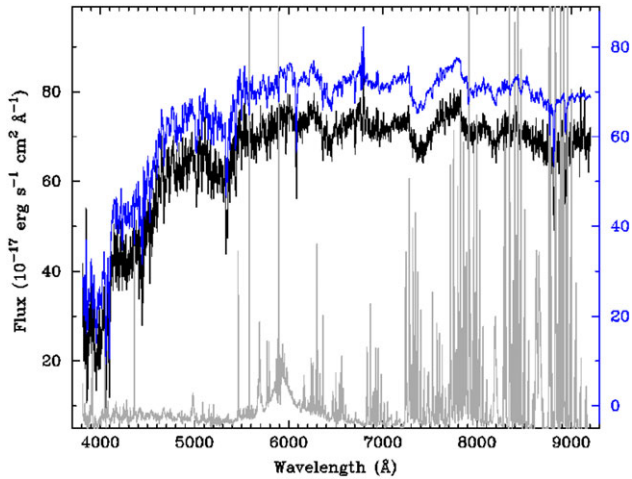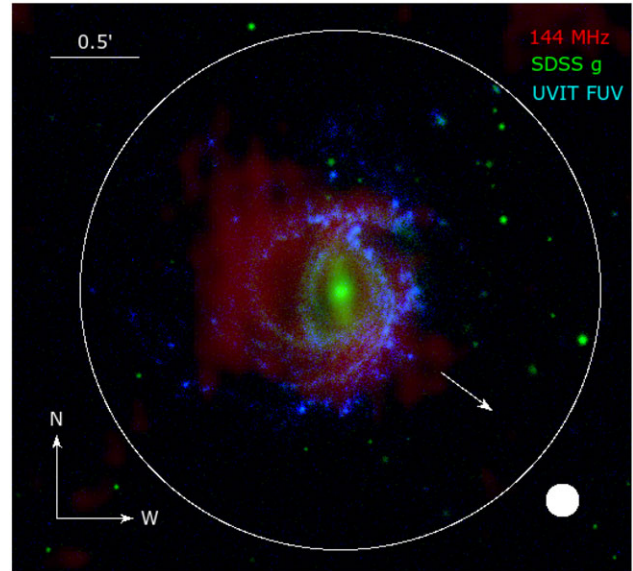
Figure 5. The spectrum *(black line)* from the nuclear region of UGC 10420 (also see Fig. 1), based on which it is classified as a LINER galaxy. The *blue* and *grey* lines represent the best-fit model to the spectrum, and emission from the sky, respectively. The model spectrum is offset along the ordinate for clarity, and the corresponding shifted axis is shown in *blue* on the right. All the data shown in this image are sourced from the SDSS database.
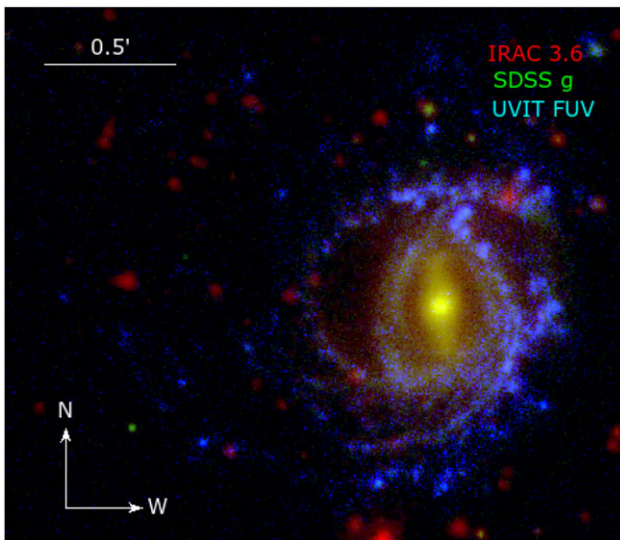

Figure 6. A composite image of UGC 10420 created using the IRAC 3.6 μm *(red)*, SDSS *g*-band *(green)* and UVIT *FUV (blue)* data, respectively. Despite different pixel sizes and depth of the three datasets, this image shows the distorted spiral arms of UGC 10420 which are likely perturbed by the interaction with the intracluster medium. It is also evident that most of the star-formation is now occurring in the outer regions of the galaxy.

Figure 7. This composite image of the UGC 10420 shows the low-frequency LOFAR radio emission *(red)*, the optical *g*-band *(green)* and the UVIT *FUV* emission *(blue)*, respectively. The synthesised radio beam is represented by the $6''$ radius circle at the bottom right. It is noteworthy that an excess of radio emission is detected in the north-western part of the galaxy, opposite to the direction of the cluster centre. The arrow points in the direction of the cluster centre.
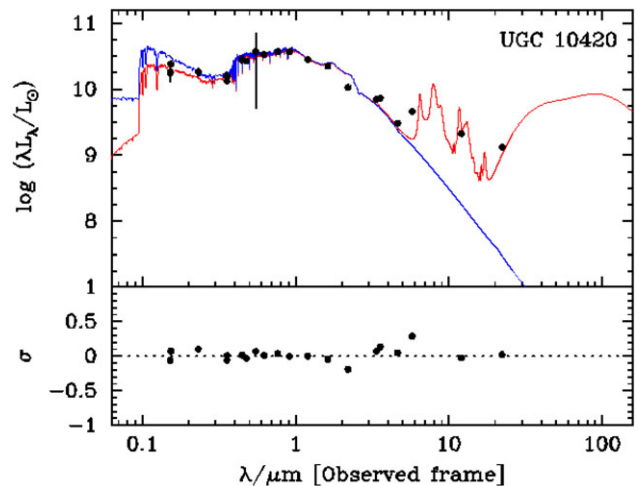
Figure 8. The integrated UV to near-infrared spectral energy distribution (SED) of the galaxy UGC 10420. In the *top panel*, photometric data from Table 8 are shown as *black points*. These data are used to fit an SED using the code MAGPHYS (da Cunha et al., 2008). The attenuated *(red line)*, and unattenuated *(blue line)* best-fit SEDs are also shown. The residuals with respect to the best-fit are shown in the *bottom panel*. Also see Table 4 for the physical parameters derived from this SED.

we use the self-contained model package called Multi-wavelength Analysis of Galaxy Physical Properties (MAGPHYS; da Cunha et al., 2008) to model the SED of UGC 10420. MAGPHYS takes the photometric data from UV to IR wavebands as input, to model the attenuated and unattenuated SED of a galaxy. It makes use of the stellar evolution models by Bruzual & Charlot (2003), assuming a Chabrier (2003) initial mass function and a Charlot & Fall (2000) attenuation law. For UGC 10420 we input the data listed in Table 1 (sans radio flux).

The output is shown in Fig. 8, and some of the derived physical parameters: SFR[d], stellar mass (M^*), dust mass (M_{Dust}) and specific star formation rate (SFR/M^*; sSFR henceforth) are listed in Table 4, respectively. The physical properties of UGC 10420 are typical of optically-selected red spiral galaxies explored in the literature (e.g. Mahajan et al., 2020).

[d]Since this SFR is based on Chabrier (2003) IMF, we have divided by 0.63 (Madau & Dickinson, 2014) to convert to the Salpeter IMF used throughout this work.

Table 4. Some physical parameters estimated from the SED of UGC 10420 fitted using the MAGPHYS code (da Cunha et al., 2008).

Parameter	Value
SFR, $M_\odot$ yr^{-1}	9.75
Stellar mass, $M^*/M_\odot$	1.8×10^{10}
Dust mass, $M_{Dust}/M_\odot$	6.8×10^6
SFR/M^*	3.4×10^{-10}

3.2. Star-forming regions

It has been shown that the detection of extended UV (XUV) emission beyond the optical extent of the galaxy is not very uncommon in nearby star-forming galaxies (e.g. Thilker et al., 2007). A comparison between this star formation far away from the centre of the galaxy, and that in the optical disc is therefore crucial in understanding star formation processes. Moreover, we are unaware of any XUV disc observed in clusters, which makes UGC 10420 a very unique galaxy.

We take advantage of the high resolution of the UVIT to get a better perspective on the individual regions which have been resolved in UGC 10420. In order to do so, we classified these regions based on their distance from the centre of the galaxy. As shown in Fig. 9(a), all regions >0.5′ from the centre of the galaxy are classified as XUV regions (blue circles) and are mostly located outside the optical disc of the galaxy. Most of these XUV regions have a faint or no optical counterpart in the SDSS g-band image. The regions which are part of the galactic disc are further sub-classified into two categories: regions which are comparable to the XUV regions in size and luminosity, and having an optical counterpart are shown in solid black circles; these are henceforth referred to as the inner regions. Secondly, the regions closer to the centre of the galaxy, which form the bulk of the emission from UGC 10420 in almost all filters are represented by dashed black circles. In total there are 21 XUV regions which are compared to 13 inner regions, while the 11 innermost regions are ignored in the following analysis because they are much more luminous (and massive) than the XUV regions. The objects marked as B1 and B2 are background galaxies and are ignored hereafter.

FUV light is emitted by stars with masses of several solar masses, and a mean age of 10 Myr ($10 - 100$ Myr), with the shortest wavelengths corresponding to the shortest timescales (Hao et al., 2011; Murphy et al., 2011; Kennicutt & Evans, 2012). The UV continuum emission from 1200 to 3200 Å is therefore an inevitable consequence of recent star formation. As a result, *FUV* luminosity is a direct tracer of recent star formation (few tens of Myr) occurring in a galaxy and can be used to estimate the rate of star formation (SFR). In this work we employ the prescription provided by Iglesias-Páramo et al. (2006):

$$\log(\mathrm{SFR}_{FUV}/\mathrm{M}_\odot\ yr^{-1}) = \log(L_{FUV}/L_\odot) - 9.51 \qquad (1)$$

where, L_{FUV} is the *FUV* luminosity of the galaxy corrected for galactic extinction (A_{FUV}). The calibration for this prescription is derived from Starburst99 models (Leitherer et al., 1999), assuming a solar metallicity and a Salpeter IMF from $0.1 - 100\ \mathrm{M}_\odot$. Galactic extinction, $A_{FUV} = 8.06 \times E(B - V)$ (Bianchi, 2011), where the

colour excess $E(B - V) = 0.0085$ for UGC 10420 is obtained from the dust reddening maps of Schlafly & Finkbeiner (2011)[e].

Fig. 9(b) shows a comparison between the SFR estimated for the XUV regions, and the inner regions using the SFR derived from UVIT data. It is notable that the XUV regions on average have lower SFR and smaller dispersion relative to similar regions closer to the centre of the galaxy. Specifically, the mean and standard deviation of SFR for the XUV regions is $0.014 \pm 0.008\ \mathrm{M}_\odot\ yr^{-1}$, relative to the value for the inner regions $0.035 \pm 0.028\ \mathrm{M}_\odot\ yr^{-1}$. The Kolmogorov-Smirnov (KS) statistical test probability (p), in favour of the hypothesis that the two distributions are drawn from the same parent sample is 1.77E-03, thus suggesting that they are disparate. Furthermore, the XUV regions have bluer *FUV − NUV* colours (Fig. 9(c); $p = 2.99$E-02), and are brighter than the inner regions (Fig. 9(d); $p = 2.09$E-03). The respective mean surface brightness value for the XUV regions is 42.8 ± 12.1 magnitude arcseconds^{-2}, relative to only 26.1 ± 7.2 magnitude arcseconds^{-2} for the inner regions.

It is noteworthy that even though a correction for internal extinction is important when converting *FUV* luminosity to SFR (e.g. Mahajan et al., 2019), in this case we are unable to do so because of the unavailability of *FIR* data, and hence the estimated SFRs may be regarded as lower limits. The result from these comparisons therefore should only be considered in a qualitative sense, assuming that the internal extinction in the XUV regions and inner regions is the same. Also, resolution effects may play a significant role in this comparison, since only the most massive star-forming regions may be resolved at the distance of UGC 10420. Most of the 'regions' considered here, therefore may be much larger than typical star-forming regions observed in nearby galaxies.

This distinction suggests that the XUV regions are statistically different from the inner regions. In our opinion, these qualitative differences suggest that they have different origins. As UGC 10420 interacts with the surrounding ICM, some of the cold atomic gas from the galaxy is stripped, leaving a wake in the direction opposite to the direction of the motion of the galaxy. The fact that the cluster centre lies diametrically opposite to the direction of the XUV tail(s) pointing towards the north-east, forms the basis of this idea. Star-forming regions beyond the optical disc have been observed in several other nearby galaxies (e.g. Cortese et al., 2007; Werk et al., 2010; Poggianti et al., 2017; Boselli et al., 2021). In particular, the galaxy IC 3476 in the Virgo cluster which is experiencing edge-on stripping is worth mentioning, since it shows HII regions in the two diametrically opposite ends of the galaxy just like UGC 10420 (see fig. 4 of Boselli et al., 2021). Also, even though we only have access to the low-frequency radio data for UGC 10420, it is evident from Fig. 7, that there is more radio emission on the trailing edge of the galaxy relative to the western side facing the cluster centre. In this situation, the inner regions are formed where the stripped gas experiences a shock, while the XUV regions are formed in the wake of the RPS gas tails.

3.3. Diffuse X-ray emission from UGC 10420

In § 2.2 we pointed out the existence of diffuse soft X-ray emission connecting two bright point-like sources and the nucleus of the

---

[e]https://irsa.ipac.caltech.edu/applications/DUST/
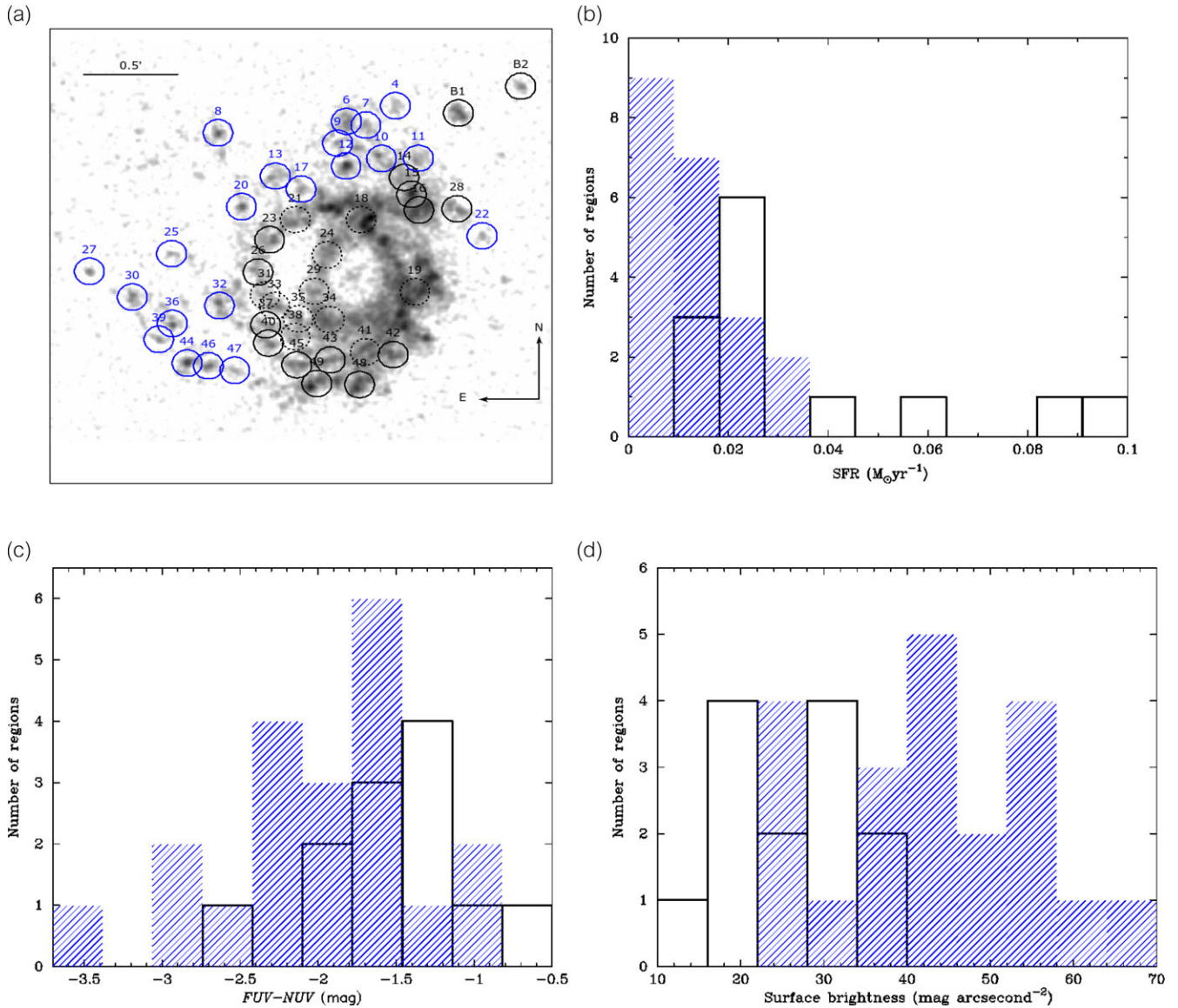
Figure 9. (a) Individual 'regions' detected by the SEXTRACTOR overlaid on the UVIT image are shown. The regions are colour-coded as follows: the regions with little to no optical emission are classified as XUV regions shown in *(blue)*, those which have optical emission in the *g*-band, and lie >0.5′ away from the optical centre as regions in galaxy *(solid black)*, respectively. Objects marked as B1 and B2 are background galaxies and not considered in our analysis. The counterparts of the latter form the bulk of the galaxy photometry in almost all the filters (and hence are very different from the smaller star-forming regions/clumps explored in this analysis) are shown as *(dashed black)* circles. The other panels show a comparison between the (b) SFR determined from *FUV* luminosity, (c) the *FUV-NUV* colour, and (d) surface brightness of the regions in the galaxy *(solid black)*, and the XUV regions *(hatched blue)*, respectively. It is evident that the XUV regions are bluer, brighter and have lower SFR relative to similar regions closer to the centre of the galaxy.

galaxy (Fig. 4 *left panel*). Here, we have tried to isolate the diffuse component in UGC 10420 and study its properties. The properties of the point sources are studied and presented in the next section. In Figure 10, we show the X-ray emission from Abell 2199 and its outskirts. The location of UGC 10420 with respect to Abell 2199 is also shown. This figure was derived from both the current observation and another *XMM-Newton* observation centered on the cluster centre. To isolate and study the properties of the diffuse X-ray emission associated with the galaxy, we have to estimate and remove the contribution of the backgrounds, cluster emission and the point sources.

We performed spectral analysis of emission within the red circular region (radius: 1.5′; label: UGC 10420) shown in Figure 10

to estimate the properties of overall diffuse X-ray emission from UGC 10420. The contribution from the two point sources in UGC 10420, shown in Figure 4, was removed using the mask image generated by the task *cheese* (Sec. 2.2). The source spectrum, the modelled background spectrum, and the spectral response of the EPIC were extracted within the red circular region encompassing the diffuse emission in UGC 10420 using the tasks *pn-spectra* (*mos-spectra*) and *pn_back* (*mos_back*). All spectra were suitably grouped using the FTOOL *grppha* (HEASoft version 6.30.1) and analysed using XSPEC version 12.12.1 (Arnaud, 1996). The diffuse background components towards UGC 10420 include the diffuse soft X-background (SXRB) and the cosmic X-ray background (CXB) which are described in detail in Tiwari & Singh (2021).
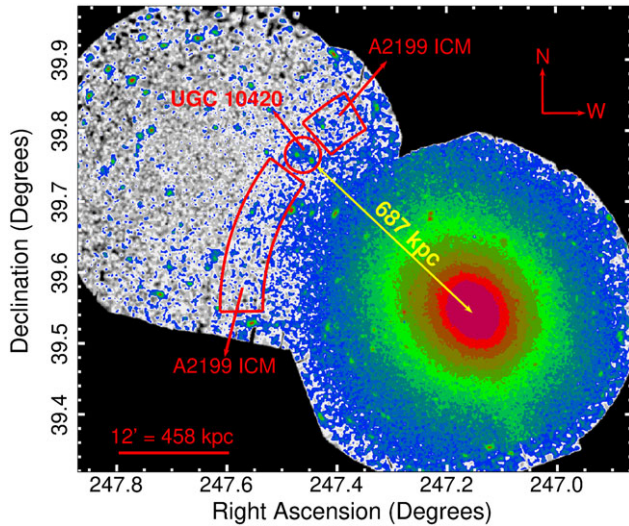
Figure 10. X-ray image in the energy band 0.4–2.0 keV showing the location of UGC 10420 within its host galaxy cluster Abell 2199. The galaxy is located at a projected distance of ~680 kpc from the X-ray peak of Abell 2199. The *small red circle* (labelled *UGC 10420*) is used for estimating the properties of the diffuse X-ray emission associated with UGC 10420. The partial annular regions sandwiching UGC 10420 (highlighted in *red* colour and labelled *A2199 ICM*) are used for estimating the properties of the Abell 2199 ICM at the location of the galaxy.

Figure 11. The total band (0.4–7.0 keV) X-ray image showing the eastern and western X-ray point sources in UGC 10420. The × symbol marks the optical centre of UGC 10420. The *solid white circles* mark the regions used for the spectral extraction and analysis of each point source.

Since UGC 10420 is located in the outskirts of Abell 2199, there is also a significant contribution from the intracluster gas. Therefore, in addition to the X-ray background components, it is also necessary to account for the emission from the ICM of Abell 2199 at the galaxy's location, when modelling its diffuse emission, as described below.

The partial annular regions sandwiching UGC 10420 shown in Figure 10 (label: *A2199 ICM*) were used to estimate the properties of the intracluster gas in the region around the galaxy. The PN, MOS1, and MOS2 spectra extracted from these annular regions were fitted jointly in the energy range 0.4–7.0 keV with the *Rosat All Sky Survey* (RASS) diffuse background spectrum using the model *constant*(apec+tbabs*(apec+apec+pegpwrlw) + tbabs*apec)*. We refer the reader to Tiwari & Singh (2021) for definitions of the individual XSPEC models and details of the background modelling. For completeness, we mention that the model component *apec+tbabs*(apec+apec+pegpwrlw)* in the expression above represents the complete X-ray background (SXRB + CXB). The second model component *tbabs*apec* represents the absorbed X-ray emission from the cluster outskirts. The *constant* factor is used to scale the model normalisation of the PN, MOS1, and MOS2 data to ensure consistency with the RASS spectral data which is in units of cts s^{-1} arcmin $^{-2}$. We fixed the total Hydrogen column density, N_H, along the line of sight to UGC 10420/Abell 2199 outskirts to 9.63×10^{19} cm^{-2}, based on the work of Willingale et al. (2013)[f]. The redshift was frozen at 0.03185. Two additional models – *gauss* (1.49 keV) and *gauss* (1.75 keV) – were used to model the instrumental background lines – the Al Kα line at ~1.49 keV for PN, MOS1, and MOS2, and the Si Kα line at ~1.75 keV for the MOS1 and MOS2 detectors – as and when required.

[f]https://www.swift.ac.uk/analysis/nhtot/
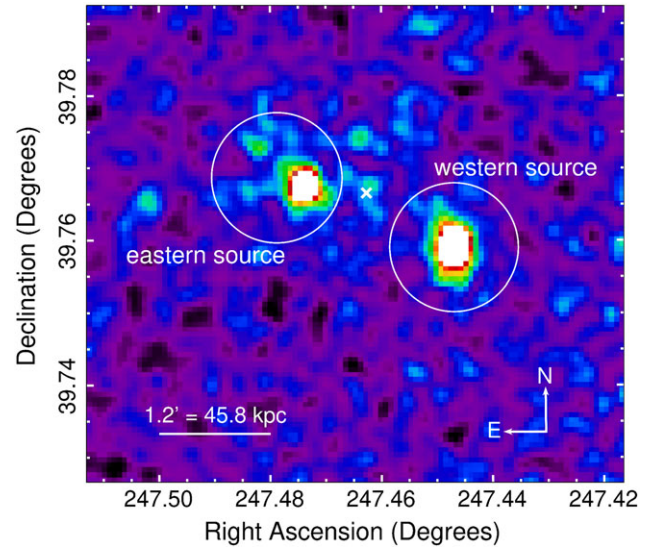
The intracluster gas at the location of UGC 10420 was found to have a temperature of $3.3^{+0.9}_{-0.7}$ keV and metallicity of ~0.2 Z$_\odot$ ($\chi^2 = 366.07$, dof $= 354$). These properties of the ICM of Abell 2199 are in agreement with previous studies by Kawaharada et al. (2010) and Mirakhor & Walker (2020).

The properties of the diffuse X-ray emission associated with UGC 10420 were then estimated by fitting the PN, MOS1, and MOS2 spectra extracted from the red circular region in Figure 10 simultaneously with the RASS background data using the model *constant*(apec+tbabs*(apec+apec+pegpwrlw) + tbabs*(apec+apec))*. The newly added *apec* component represents emission from the hot interstellar gas in the galaxy. The other model components have the same definitions as described previously. Here, the spectral parameters for the X-ray background, and the temperature and abundance of the Abell 2199 ICM were fixed based on the results of the spectral analysis mentioned above. The energy range 0.4–7.0 keV was used for the spectral fitting. We found the hot gas in UGC 10420 to have a temperature of $0.24^{+0.09}_{-0.06}$ keV, with the metal abundance, Z, frozen at the solar value ($\chi^2 = 104.53$, dof$= 114$). If the abundance was left free to vary during the fit, we obtained Z $= 0.8$ Z$_\odot$ with the gas temperature unchanged, but the errors in the abundance could not be constrained due to low number of counts.

3.4. X-ray emission from the two hot spots and nuclear region

Spectral analysis of the two bright point sources in UGC 10420 was carried out by extracting spectra from the circular regions shown in Figure 11 to estimate their general properties. These relatively large regions, extending beyond the actual size of the detected sources, were used so as to enclose enough counts to make the spectral modelling possible. Since these circular regions also enclose the diffuse emission from the cluster and galaxy, we accounted for these contributions in the spectral analysis as described above. The spectrum of each point source was well fitted

Table 5. Properties of the two X-ray point sources in UGC 10420. The errors in photon index, flux, and luminosity are quoted at 90 per cent confidence level.

	R.A. (J2000)	Dec. (J2000)	Photon index (α)	χ^2 (dof)	Flux (0.4–7.0 keV) erg cm^{-2} s^{-1}	Luminosity (0.4–7.0 keV) erg s^{-1}
Eastern source	16h29m53.92s	+39d46m01.67s	$1.8^{+0.3}_{-0.2}$	20.45 (34)	$2.6 \pm 0.4 \times 10^{-14}$	$6.7 \pm 1.1 \times 10^{40}$
Western source	16h29m47.41s	+39d45m31.78s	1.6 ± 0.2	61.13 (58)	$4.9 \pm 0.5 \times 10^{-14}$	$1.2 \pm 0.1 \times 10^{41}$

Table 6. Total unabsorbed X-ray flux (F_X in erg cm^{-2} s^{-1}) and luminosity (L_X in erg s^{-1}) estimates of UGC 10420. The errors are quoted at 90 per cent confidence level.

Aperture radius	Soft band (0.4–2.0 keV)	Hard band (2.0–7.0 keV)	Total band (0.4–7.0 keV)
1.5′	F_X: $3.7 \pm 0.5 \times 10^{-14}$	F_X: $3.6^{+0.4}_{-0.5} \times 10^{-14}$	F_X: $7.3 \pm 0.9 \times 10^{-14}$
	L_X: $9.3 \pm 1.1 \times 10^{40}$	L_X: $9.1 \pm 0.9 \times 10^{40}$	L_X: $1.8 \pm 0.2 \times 10^{41}$
0.8′	F_X: $2.5 \pm 0.3 \times 10^{-14}$	F_X: $2.2 \pm 0.3 \times 10^{-14}$	F_X: $4.7 \pm 0.6 \times 10^{-14}$
	L_X: $6.2 \pm 0.7 \times 10^{40}$	L_X: $5.7^{+0.6}_{-0.8} \times 10^{40}$	L_X: $1.2 \pm 0.1 \times 10^{41}$

by a power-law[g] in the energy range 0.4–7.0 keV. The unabsorbed flux (luminosity) of each point source was estimated by convolving the *powerlaw* model with the XSPEC model *cflux* (*clumin*) after freezing the power-law model normalisation. The results of the spectral analysis and the derived properties of the two point sources are given in Table 5.

The unabsorbed X-ray flux and luminosity of the entire galaxy (hot spots + diffuse emission) were estimated within two circular apertures of radii 0.8′ and 1.5′ centred at the optical centre of the galaxy (see Figure 4). In order to do so, the PN, MOS1, and MOS2 spectra extracted within the 1.5′ radius aperture were simultaneously fitted with the RASS data using the model *constant* (apec+tbabs*(apec+apec+pegpwrlw) + tbabs*(apec+* **apec** *+* **powerlaw** *+* **powerlaw***))*. The highlighted model component represents the total X-ray emission – point sources + diffuse – from UGC 10420. Here, *apec* represents the diffuse emission from UGC 10420, and the two *powerlaw* components model the emission from the two point sources in UGC 10420 which lie within the aperture of radius 1.5′. For modelling the X-ray spectrum within the smaller aperture of radius 0.8′, we used only one *powerlaw* model since only the eastern point source falls within this aperture. The X-ray flux in the two apertures was then estimated by convolving the *apec + powerlaw + powerlaw* component with the XSPEC model *cflux*. Similarly, the total X-ray luminosity was estimated using the XSPEC convolution model *clumin*. The total X-ray flux and luminosity values for the two apertures in the soft, hard, and total bands are reported in Table 6.

A limit to the soft X-ray flux from the nuclear region, which is not fully resolved, was estimated from the PN data in the soft band and using a circular region with a radius of 9 arcsec. Scaling the estimated PN background to the same size, we obtain a 3σ upper limit on the soft emission from the nuclear region around the optical centre to be ~0.004 counts s^{-1}. Assuming the central source to have a photon index of 2, this limit translates to a flux

of $5.4\,10^{-15}$ erg cm^{-2} s^{-1} in the soft energy band, giving a 3σ limit on luminosity of $1.4\,10^{40}$ ergs s^{-1} for an AGN like source in the centre.

4. Discussion

In this paper we have presented the UVIT *FUV* data and ancillary data in other wavebands for the spiral galaxy UGC 10420, a member of the cluster Abell 2199. Our analysis shows that this galaxy, at a projected distance of ~680 kpc from the cluster's centre is being ram-pressure stripped by the ICM of the cluster. It is notable that the l.o.s. velocity offset of UGC 10420 with respect to the mean velocity of Abell 2199 is only ~372 km s^{-1}, which is much smaller than the velocity dispersion of the cluster. This, together with the *FUV* observations presented in this work, suggests that UGC 10420 must be moving with a very high speed towards the cluster centre, in a direction normal to the l.o.s. As a consequence of stripping, the outer spiral arms of the galaxy are being removed and turned into what looks like a wake of star-forming knots on the south-eastern side of the galaxy (Fig. 1). These observations agree with the simulations of RPS galaxies suggesting that the SFR increases in the gaseous wake of the galaxy rather than the disc itself, and hence is strongly dependant on the density of the surrounding ICM (Kapferer et al., 2009).

There is an increasing consensus building up in the recent literature that most of the enhanced star formation in RPS galaxies is observed on the 'leading edge' of the galaxies (Gavazzi et al., 2015; Vulcani et al., 2018; Hess et al., 2022; Roberts et al., 2022a). Such galaxies, showing an unambiguous tail of material stripped from the disc are often called the 'jellyfish galaxies' and are considered to be a product of RPS in clusters. It is believed that the stripped gas must cross the entire galaxy disc before leaving it and therefore is more likely to cause instabilities and turbulence, which in turn triggers starburst in jellyfish galaxies (Boselli et al., 2022). Several examples of such jellyfish galaxies have been observationally discovered (Poggianti et al., 2016; Vulcani et al., 2018; Safarzadeh & Loeb, 2019; Lee et al., 2020; Cramer et al., 2021; Roberts et al., 2022b). The *FUV* observations of UGC 10420, showing intense star-forming knots on the western side of the disc (Fig. 1), also favours this scenario.

In order to test the significance of the increase in the SFR of UGC 10420, we adopted the following SFR main sequence relation derived by Speagle et al. (2014) as a function of stellar mass and cosmic time:

$$\log \text{SFR}(M^*, t) = (0.84 - 0.026t)\log M^* - (6.51 - 0.11t),$$

where, t is the age of the Universe (Gyr) at the redshift of the galaxy. In line with many other observations in the literature (Lee et al., 2022, and references therein), we find that the SED derived SFR of UGC 10420 is at least a factor of nine larger than that expected for star-forming field galaxies of similar mass at $z \sim 0.03$.

---

[g]The power-law photon spectrum has the form $KE^{-\alpha}$, where α (dimensionless) is the photon index of the power-law, and K is the normalisation in units of photons keV^{-1} cm^{-2} s^{-1} at 1 keV.

The observations presented in this work are also in good agreement with a recent study of cluster galaxies in the EAGLE simulations, where Troncoso-Iribarren et al. (2020) have shown that properties such as the SFR, star formation efficiency and ISM pressure are enhanced on the leading edge of the normal star-forming galaxies. On the other hand, an increase in the gas particles is observed on the 'trailing edge' of these galaxies, suggesting removal of cold gas via RPS. Similar results were obtained by Boselli et al. (2021), who presented hydrodynamical simulations of the RPS galaxy IC 3476 along with its multi-wavelength data. The fact that UGC 10420 seems to have more gas present on the trailing edge (Fig. 7), and an asymmetric distribution of star-forming regions, supports the results from the simulations.

These results from simulations were recently tested observationally by Roberts et al. (2022b), who found them to agree with the resolved analysis of the integral field spectroscopic data of 29 jellyfish galaxies. A case study of IC 3949 presented by these authors is further evidence in favour of a scenario where the increased ISM pressure on the leading edge compresses the atomic Hydrogen and turns it into molecular gas, thereby triggering a localised burst of star formation. Troncoso-Iribarren et al. (2020) also showed that this effect is most pronounced in galaxies in the stellar mass range of $10^{9.5} - 10^{10.5}\ M_\odot$, which conveniently includes UGC 10420 (Table 4).

An examination of the individual XUV star-forming regions (defined in Sec. 3.2) shows that they are statistically brighter than their counterparts at lower galactocentric distances and have relatively bluer *FUV-NUV* colours and lower SFR. These observations are in agreement with the results of Werk et al. (2010), who analysed the HI and *FUV* data for some nearby star-forming galaxies. Werk et al. (2010) found that 8%–11% of emission-line point sources, near star-forming galaxies in their sample, are HII regions associated with the extended UV disc of the galaxies.

Any environmental mechanism which influences the gas content of a galaxy, thereby affecting its SFR, can potentially impact the AGN activity as well. In order to test this hypothesis, Peluso et al. (2022) have recently exploited the integral field data for 115 RPS galaxies from MANGA and MUSE. Peluso et al. (2022) find that AGN fraction among RPS galaxies is higher than their non-RPS counterparts. Furthermore, the incidence of optical AGN (classifiable using the BPT diagnostics) is 51% among massive ($M^* \geq 10^{10} M_\odot$) RPS galaxies. It therefore comes as no surprise that UGC 10420 is optically classified as a LINER (Toba et al., 2014). On the contrary, evidence has been presented in the literature to show that presence of a low-ionisation emission region may not always correspond to nuclear activity (e.g. Belfiore et al., 2016). Interested readers are directed to Boselli et al. (2022, and references therin), for a detailed discussion on the subject, while deeper and high resolution data would be required to confirm presence of AGN in UGC 10420.

Analysis of archival X-ray data shows that UGC 10420 lies just at the edge of the X-ray emitting region of Abell 2199. Two bright X-ray sources, a few tens of kpc away from the centre of the galaxy without any optical counterpart are clearly visible, along with very faint emission from the central region of the galaxy. Such bright sources (hot spots, hereafter), are reminiscent of those generally observed around bright active galactic nuclei like Pictor A. Although such hot spots are often connected with a jet seen as faint diffuse emission (Hardcastle et al., 2016), such is not the case with UGC 10420. The eastern hot spot appears to be embedded in diffuse radio emission at that location as has been seen in Pictor A

(Thimmappa et al., 2021). It should be noted that the nucleus in Pictor A is about 20 times brighter than the hot spots (Hardcastle et al., 2016), while almost the reverse is true here.

The X-ray spectrum of the two hot spots in UGC 10420 are well fitted by a power-law with photon index of $1.8^{+0.3}_{-0.2}$ and 1.6 ± 0.2 for the eastern and western source, respectively. The luminosities of these hot spots are similar to the hot spots in Pictor A, while the nucleus is an order of magnitude weaker. If confirmed with deeper *Chandra* observations with higher resolution, this would be the first case of hot spots associated with such a weak nucleus. This also indicates that we do not find any evidence of enhancement in the nuclear activity in the galaxy due to the RPS process, which has a luminosity typical of low-activity nucleus in LINERS.

A careful analysis of diffuse X-ray emission indicates that the hot galactic plasma in UGC 10420 has a temperature of $0.24^{+0.09}_{-0.06}$ keV, consistent with that observed in spiral galaxies (e.g. Li et al., 2008; Mineo et al., 2012). Also, the X-ray luminosity of the diffuse gas component in UGC 10420 is $1.8 \pm 0.9 \times 10^{40}$ erg s^{-1} (0.4–2.0 keV), which is typical of spiral galaxies (Tyler et al., 2004; Owen & Warwick, 2009; Mineo et al., 2012). This also indicates that the RPS has no effect on the hot gas in the galaxy.

In a nutshell, multi-wavelength analysis of UGC 10420 confirms that it is a RPS galaxy which is undergoing a short-lived phase of intense star formation, as it interacts with the ICM in the cluster Abell 2199. While the star-forming knots on the western side of the disc are formed as a consequence of the compression of ISM of the galaxy due to RPS, the star formation on the eastern side is part of the wake which comprises loosely bound or ejected gas from the galaxy. References from the literature suggest that deep narrow-band and radio continuum imaging of UGC 10420 should produce further evidence to support the ideas presented in this paper. Although it is worth mentioning that UGC 10420 is unique not only because of the asymmetric distribution of star-forming regions, but also due to its status as an XUV disc galaxy hosted by a cluster.

5. Epilogue

Although the multi-wavelength analysis of the data for UGC 10420 has thrown some light on the evolution of this and such similar objects, it is worth mentioning the paucity of narrow-band data. We believe narrow-band imaging (Hα), sensitive to the presence of massive O stars would be a key to probing the XUV star-formation in this galaxy. Also, continuum and HI emission and molecular gas observations can throw light on the distribution of gas in and around the galaxy and may prove very helpful in understanding the role of RPS in the evolution of UGC 10420, just like other RPS galaxies observed in clusters (e.g. Smith et al., 2010; Werk et al., 2010; Cortese et al., 2007; Yagi et al., 2010; Roman-Oliveira et al., 2019; Boselli et al., 2021).

(Bengaluru), IUCAA (Pune), TIFR (Mumbai), several centres of ISRO, and the Canadian Space Agency (CSA). This research has made use of the NASA/IPAC Infrared Science Archive, which is funded by the National Aeronautics and Space Administration and operated by the California Institute of Technology. The TOPCAT software (Taylor, 2005) was used for some of the analysis presented in this paper. This publication makes use of data products from the Wide-field Infrared Survey Explorer, which is a joint project of the University of California, Los Angeles, and the Jet Propulsion Laboratory/California Institute of Technology, funded by the National Aeronautics and Space Administration. This dataset or service is made available by the Infrared Science Archive (IRSA) at IPAC, which is operated by the California Institute of Technology under contract with the National Aeronautics and Space Administration. We acknowledge the use of LOFAR data in accordance with the credits given on https://lofar-surveys.org/credits.html, and SDSS data given on https://www.sdss.org/collaboration/citing-sdss/. The X-ray data were downloaded from the High Energy Astrophysics Science Archive Research Center (HEASARC), maintained by NASA's Goddard Space Flight Center. This research has made use of SAOImageDS9, developed by Smithsonian Astrophysical Observatory, and the HEASoft FTOOLS (http://heasarc.gsfc.nasa.gov/ftools).

Data Availability. Not applicable.

References

Abolfathi B., et al., 2018, ApJS, 235, 42

Arnaud K. A., 1996, in Jacoby G. H., Barnes J., eds, Astronomical Society of the Pacific Conference Series Vol. 101, Astronomical Data Analysis Software and Systems V. p. 17

Baldwin J. A., Phillips M. M., Terlevich R., 1981, PASP, 93, 5

Balogh M., et al., 2004, MNRAS, 348, 1355

Bekki K., 2014, MNRAS, 438, 444

Bekki K., Couch W. J., 2003, ApJ, 596, L13

Belfiore F., et al., 2016, MNRAS, 461, 3111

Bianchi L., 2011, Ap&SS, 335, 51

Boselli A., Cortese L., Boquien M., Boissier S., Catinella B., Gavazzi G., Lagos C., Saintonge A., 2014, A&A, 564, A67

Boselli A., et al., 2021, A&A, 646, A139

Boselli A., Fossati M., Sun M., 2022, A&A Rev., 30, 3

Bruzual G., Charlot S., 2003, MNRAS, 344, 1000

Buta R. J., 2019, MNRAS, 488, 590

Cattorini F., Gavazzi G., Boselli A., Fossati M., 2022, arXiv e-prints, p. arXiv:2211.06437

Chabrier G., 2003, ApJ, 586, L133

Charlot S., Fall S. M., 2000, ApJ, 539, 718

Cortese L., et al., 2007, MNRAS, 376, 157

Cowie L. L., Songaila A., 1977, Nature, 266, 501

Cramer W. J., et al., 2021, ApJ, 921, 22

Crowl H. H., Kenney J. D., van Gorkom J. H., Chung A., Rose J. A., 2006, in American Astronomical Society Meeting Abstracts. p. 211.11

Cybulski R., Yun M. S., Fazio G. G., Gutermuth R. A., 2014, MNRAS, 439, 3564

Dressler A., 1980, ApJ, 236, 351

Fraser-McKelvie A., et al., 2020, MNRAS, 495, 4158

Gavazzi G., O'Neil K., Boselli A., van Driel W., 2006, A&A, 449, 929

Gavazzi G., et al., 2015, A&A, 576, A16

Gil de Paz A., et al., 2007, ApJS, 173, 185

Gunn J. E., Gott J. Richard I., 1972, ApJ, 176, 1

Haines C. P., et al., 2009, ApJ, 704, 126

Hao C.-N., Kennicutt R. C., Johnson B. D., Calzetti D., Dale D. A., Moustakas J., 2011, ApJ, 741, 124

Hardcastle M. J., et al., 2016, MNRAS, 455, 3526

Hess K. M., Kotulla R., Chen H., Carignan C., Gallagher J. S., Jarrett T. H., Kraan-Korteweg R. C., 2022, arXiv eprints, p. arXiv:2209.05605

Iglesias-Páramo J., et al., 2006, ApJS, 164, 38

Joye W. A., Mandel E., 2003, in Payne H. E., Jedrzejewski R. I., Hook R. N., eds, Astronomical Society of the Pacific Conference Series Vol. 295, Astronomical Data Analysis Software and Systems XII. p. 489

Kapferer W., Sluka C., Schindler S., Ferrari C., Ziegler B., 2009, A&A, 499, 87

Kawaharada M., Makishima K., Kitaguchi T., Okuyama S., Nakazawa K., Fukazawa Y., 2010, PASJ, 62, 115

Kennicutt R. C., Evans N. J., 2012, ARA&A, 50, 531

Kumar A., et al., 2012, in Takahashi T., Murray S. S., den Herder J.-W. A., eds, Society of Photo-Optical Instrumentation Engineers (SPIE) Conference Series Vol. 8443, Space Telescopes and Instrumentation 2012: Ultraviolet to Gamma Ray. p. 84431N (arXiv:1208.4670), doi: 10.1117/12.924507

Kuntz K. D., Snowden S. L., 2008, A&A, 478, 575

Lee J., Kimm T., Katz H., Rosdahl J., Devriendt J., Slyz A., 2020, ApJ, 905, 31

Lee J. H., Lee M. G., Mun J. Y., Cho B. S., Kang J., 2022, ApJ, 931, L22

Leitherer C., et al., 1999, ApJS, 123, 3

Li J.-T., Li Z., Wang Q. D., Irwin J. A., Rossa J., 2008, MNRAS, 390, 59

Madau P., Dickinson M., 2014, ARA&A, 52, 415

Mahajan S., Raychaudhury S., 2009, MNRAS, 400, 687

Mahajan S., Haines C. P., Raychaudhury S., 2010, MNRAS, 404, 1745

Mahajan S., Raychaudhury S., Pimbblet K. A., 2012, MNRAS, 427, 1252

Mahajan S., Ashby M. L. N., Willner S. P., Barmby P., Fazio G. G., Maragkoudakis A., Raychaudhury S., Zezas A., 2019, MNRAS, 482, 560

Mahajan S., et al., 2020, MNRAS, 491, 398

Mahajan S., Singh K. P., Postma J. E., Pradeep K. G., George K., Côté P., 2022, PASA, 39, e048

Mahdavi A., Geller M. J., 2001, ApJ, 554, L129

Mineo S., Gilfanov M., Sunyaev R., 2012, MNRAS, 426, 1870

Mirakhor M. S., Walker S. A., 2020, MNRAS, 497, 3943

Moore B., Katz N., Lake G., Dressler A., Oemler A., 1996, Nature, 379, 613

Murphy E. J., et al., 2011, ApJ, 737, 67

Owen R. A., Warwick R. S., 2009, MNRAS, 394, 1741

Peluso G., et al., 2022, ApJ, 927, 130

Poggianti B. M., et al., 2016, AJ, 151, 78

Poggianti B. M., et al., 2017, ApJ, 844, 48

Porter S. C., Raychaudhury S., 2005, MNRAS, 364, 1387

Postma J. E., Leahy D., 2017, PASP, 129, 115002

Postma J. E., Leahy D., 2021, Journal of Astrophysics and Astronomy, 42, 30

Rines K. J., Geller M. J., Diaferio A., Hwang H. S., 2016, ApJ, 819, 63

Roberts I. D., van Weeren R. J., Timmerman R., Botteon A., Gendron-Marsolais M., Ignesti A., Rottgering H. J. A., 2022a, A&A, 658, A44

Roberts I. D., et al., 2022b, ApJ, 941, 77

Roman-Oliveira F. V., Chies-Santos A. L., Rodríguez del Pino B., Aragón-Salamanca A., Gray M. E., Bamford S. P., 2019, MNRAS, 484, 892

Safarzadeh M., Loeb A., 2019, MNRAS, 486, L26

Schlafly E. F., Finkbeiner D. P., 2011, ApJ, 737, 103

Shimwell T. W., et al., 2022, A&A, 659, A1

Singh K. P., et al., 2014, in Takahashi T., den Herder J.-W. A., Bautz M., eds, Society of Photo-Optical Instrumentation Engineers (SPIE) Conference Series Vol. 9144,

Space Telescopes and Instrumentation 2014: Ultraviolet to Gamma Ray. p. 91441S, doi: 10.1117/12.2062667

Smith R. J., et al., 2010, MNRAS, 408, 1417

Song H., Hwang H. S., Park C., Tamura T., 2017, ApJ, 842, 88

Speagle J. S., Steinhardt C. L., Capak P. L., Silverman J. D., 2014, ApJS, 214, 15

Steinhauser D., Schindler S., Springel V., 2016, A&A, 591, A51

Tandon S. N., et al., 2017, AJ, 154, 128

Tandon S. N., et al., 2020, AJ, 159, 158

Taylor M. B., 2005, in Shopbell P., Britton M., Ebert R., eds, Astronomical Society of the Pacific Conference Series Vol. 347, Astronomical Data Analysis Software and Systems XIV. p. 29

Thilker D. A., et al., 2007, ApJS, 173, 538

Thimmappa R., Stawarz Ł., Pajdosz-Śmierciak U., Balasubramaniam K., Marchenko V., 2021, ApJ, 921, 44

Tiwari J., Singh K. P., 2021, MNRAS, 500, 5524

Toba Y., et al., 2014, ApJ, 788, 45

Tonnesen S., Bryan G. L., 2009, ApJ, 694, 789

Toomre A., Toomre J., 1972, ApJ, 178, 623

Troncoso-Iribarren P., Padilla N., Santander C., Lagos C. D. P., García-Lambas D., Rodríguez S., Contreras S., 2020, MNRAS, 497, 4145

Tyler K., Quillen A. C., LaPage A., Rieke G. H., 2004, ApJ, 610, 213

Vulcani B., Poggianti B. M., Finn R. A., Rudnick G., Desai V., Bamford S., 2010, ApJ, 710, L1

Vulcani B., et al., 2018, ApJ, 866, L25

Werk J. K., et al., 2010, AJ, 139, 279

Willingale R., Starling R. L. C., Beardmore A. P., Tanvir N. R., O'Brien P. T., 2013, MNRAS, 431, 394

Wright E. L., et al., 2010, AJ, 140, 1868

Yagi M., et al., 2010, AJ, 140, 1814

da Cunha E., Charlot S., Elbaz D., 2008, MNRAS, 388, 1595